Chemical Science

ROYAL SOCIETY OF CHEMISTRY

EDGE ARTICLE

View Article Online
View Journal | View Issue



Cite this: *Chem. Sci.*, 2024, **15**, 336

All publication charges for this article have been paid for by the Royal Society of Chemistry



# Endogenous metal-ion dynamic nuclear polarization for NMR signal enhancement in metal organic frameworks†

Ilia B. Moroz, [a] Yishay Feldman,[b] Raanan Carmieli,[b] Xinyu Liu[c] and Michal Leskes *[a]

Rational design of metal–organic framework (MOF)-based materials for catalysis, gas capture and storage, requires deep understanding of the host–guest interactions between the MOF and the adsorbed molecules. Solid-State NMR spectroscopy is an established tool for obtaining such structural information, however its low sensitivity limits its application. This limitation can be overcome with dynamic nuclear polarization (DNP) which is based on polarization transfer from unpaired electrons to the nuclei of interest and, as a result, enhancement of the NMR signal. Typically, DNP is achieved by impregnating or wetting the MOF material with a solution of nitroxide biradicals, which prevents or interferes with the study of host–guest interactions. Here we demonstrate how Gd(III) ions doped into the MOF structure, LaBTB (BTB = 4,4′,4″-benzene-1,3,5-triyl-trisbenzoate), can be employed as an efficient polarization agent, yielding up to 30-fold $^{13}C$ signal enhancement for the MOF linkers, while leaving the pores empty for potential guests. Furthermore, we demonstrate that ethylene glycol, loaded into the MOF as a guest, can also be polarized using our approach. We identify specific challenges in DNP studies of MOFs, associated with residual oxygen trapped within the MOF pores and the dynamics of the framework and its guests, even at cryogenic temperatures. To address these, we describe optimal conditions for carrying out and maximizing the enhancement achieved in DNP-NMR experiments. The approach presented here can be expanded to other porous materials which are currently the state-of-the-art in energy and sustainability research.

Received 6th July 2023
Accepted 23rd November 2023

DOI: 10.1039/d3sc03456a

rsc.li/chemical-science

## Introduction

Metal–Organic Frameworks (MOFs) are crystalline microporous materials that have attracted considerable interest in the last few decades due to their ultrahigh adsorption capacity, structure and composition tunability which can be tailored for various applications.[1–4] The combination of these unique properties has made them promising candidates in green chemistry and alternative energy processes including $CO_2$ capture,[5–7] air and water purification,[8–10] selective catalysis,[11–14] conversion and storage of alternative fuels such as $H_2$ and $CH_4$.[15–17]

The crystal structure of MOFs is commonly determined by diffraction techniques.[18] However, diffraction methods do not provide information about the local structure of the metal centers or the functionalized organic linkers. They are also not suitable for probing interactions between the MOF and the chemical species within its pores (so-called host–guest interactions). Understanding host–guest interactions is essential for improving the performance of MOF-based materials. These questions have been successfully addressed by solid-state NMR spectroscopy as the nuclear resonance frequency and various magnetic interactions provide information on the local environment of the nuclei.[19–26] Furthermore, as NMR does not require the presence of long-range order it is a great complementary tool to diffraction. Nevertheless, the use of solid-state NMR spectroscopy is limited due to its inherently low sensitivity.[27] This hinders detection of nuclei that are present in small quantities (for example, in active sites or adsorbed gases), having low natural abundance ($^{13}C$, $^{15}N$, $^{17}O$, *etc.*) or exhibiting broad NMR lines (such as the nuclei of many of the metal ions).

The sensitivity issue has been successfully addressed by the development of hyperpolarization techniques such as dynamic nuclear polarization (DNP).[28,29] In DNP the high spin polarization of electrons is transferred to nuclei of interest through

[a]*Department of Molecular Chemistry and Materials Science, Weizmann Institute of Science, Rehovot 76100, Israel. E-mail: michal.leskes@weizmann.ac.il*

[b]*Department of Chemical Research Support, Weizmann Institute of Science, Rehovot 76100, Israel*

[c]*Yusuf Hamied Department of Chemistry, University of Cambridge, Lensfield Road, Cambridge, CB2 1EW, UK*

† Electronic supplementary information (ESI) available: X-ray diffraction patterns of as-synthesized samples, SEM images, additional EPR and NMR spectra, nuclear relaxation times, DNP enhancements and build-up times. See DOI: https://doi.org/10.1039/d3sc03456a

microwave irradiation and electron-nuclear couplings. This leads to significant enhancement of the NMR signals expanding the range of applications of NMR spectroscopy. In a standard DNP experiment, the investigated material is impregnated with a solution of an exogenous polarizing agent that is the source of unpaired electrons.[30,31] Exogenous DNP has been utilized to characterize the surface functionalities of MOFs and probe their binding to metal ions or peptides.[32–34] Moreover, DNP has enabled very challenging NMR experiments, such as acquisition of ultrawide-line $^{195}$Pt NMR spectra of $Pt^{2+}$ sites in UiO-66 and MOF-253;[35] detection of highly insensitive $^{17}$O nuclei at natural abundance (0.037%) for metal-oxo clusters representing nodes of MIP-206,[36] and recording of $^{27}$Al–$^{13}$C 2D correlations for Al-based MIL-100 with significantly reduced experimental time.[37] The drawback of exogenous DNP is a possible alteration of the sample *via* reaction with the solvent or the polarization agent, resulting in lower DNP efficiency and changes to the sample's composition.[38,39] Furthermore, exogenous DNP is not optimal for probing host–guest interactions in MOFs as the pores are impregnated and not available for guests.

We and others have recently demonstrated that paramagnetic metal ions introduced into the structure of inorganic and molecular solids[40–48] can be used as efficient polarizing agents in magic angle spinning (MAS)-DNP. This alternative DNP approach called endogenous metal-ion DNP (MIDNP) has been applied to a broad range of technologically relevant solids used in batteries, catalysis and fuel cells. In contrast to exogenous DNP, the MIDNP approach can provide an alternative and powerful tool for boosting NMR sensitivity while enabling detection of host–guest interactions in MOFs as the pores would remain available for guests. Nevertheless, to date MIDNP applications have been mostly limited to condensed inorganic solids such as oxides and phosphates.

Here we describe the first implementation of MIDNP to a porous organic-inorganic system. We demonstrate how the endogenous MIDNP approach can be expanded to porous frameworks such as MOFs. As a test case we utilize Gd(III) ions introduced as dopants in a lanthanide-based MOF structure, LnBTB, where BTB stands for 4,4′,4″-benzene-1,3,5-triyl-trisbenzoate. LnBTB MOFs were shown to have good moisture and chemical stability and applications in gas separation[49,50] and catalysis.[51,52] This structure has previously been obtained for eleven rare-earth metal ions, including diamagnetic La(III) and paramagnetic Gd(III) which have the same charge and similar ionic radius.[53] Therefore, it seemed plausible to synthesize a bimetallic MOF, where some of the La(III) ions in the framework will be replaced by Gd(III), the latter playing the role of the polarizing agent. Moreover, LnBTB represents a rare example of the rare-earth-based coordination polymers with a permanent porosity, *i.e.* the pore structure does not collapse upon departure of guest molecules, allowing to study MOF interactions with guests.[53]

We provide detailed characterization of the Gd(III) dopants and discuss the underlying mechanism of DNP. We investigate the effects of Gd(III) concentration, molecular oxygen trapped in the pores, and the MOF mobility on the MIDNP performance. Furthermore, we describe protocols for maximizing MIDNP efficacy and enabling significant time saving in the detection of $^{13}$C spectra by increasing the sensitivity by 3 orders of magnitude. Finally, we explore the potential of MIDNP for polarizing guests introduced into the MOF and interacting with it.

## Results and discussion

### Synthesis of Gd-LaBTB MOF

Gd(III)-doped LaBTB samples were synthesized with various concentrations of Gd(III) dopant *via* solvothermal synthesis using cyclohexanol-water solvent mixture.[53] Powder X-ray diffraction patterns (Fig. S1†) of the as-synthesized samples confirm the formation of a pure MOF phase. The obtained MOF crystals are micron-sized and have a needle-like shape (see Fig. S2†), in agreement with published results.[53] The incorporation of Gd into the LaBTB structure had no discernible impact on the $CO_2$ adsorption properties of the MOF, as nearly identical $CO_2$ adsorption–desorption isotherms were obtained for both the undoped and Gd-doped LaBTB samples (see Fig. S3†). For electron paramagnetic resonance (EPR) and DNP NMR studies, as-synthesized samples were activated at 423 K in vacuum, and their X-ray diffraction patterns were recorded under Ar atmosphere showing no indication of structure decomposition upon activation (Fig. 1a). Note that an alternative synthetic route described in the literature,[49] where a mixture of DMF, methanol and water solvents is used, was chosen at first due to a significantly faster synthesis (2 days *vs.* 5 days). However, this procedure led to formation of lanthanum formate $La(HCO_2)_3$ impurities (see Fig. S4†), with both the MOF and the formate phase doped with Gd(III), complicating the evaluation of the DNP performance. Therefore, unless otherwise stated, the following DNP NMR measurements were performed on the formate-free phase-pure MOF samples.

The exact La/Gd ratio in the formate-free Gd-LaBTB samples was determined by energy dispersive X-ray fluorescence (EDXRF) analysis. For all samples, the resulting La/Gd ratio was lower than the expected value, suggesting more Gd(III) was doped into the structure of LaBTB than was initially targeted (see Table S1†). The obtained La/Gd ratio was recalculated into the volumetric concentration taking into account the unit cell parameters reported for LaBTB,[49] with the assumption that the low dopant concentration does not affect the unit cell volume. The results reported here refer to the experimentally determined Gd(III) concentrations, namely 2.5, 6, 10, 23.5 and 47 mM. The samples are labeled as *X* Gd-LaBTB, where *X* is the concentration of Gd(III) determined from EDXRF.

### EPR studies of Gd(III) dopant

The Gd(III) dopant in LaBTB was characterized by continuous-wave (CW) EPR spectroscopy. The as-synthesized Gd-LaBTB samples measured in air exhibit a very weak EPR signal at 9.4 GHz (X-band), possibly due to the presence of paramagnetic molecular oxygen inside the pores causing increased relaxation and broadening of the EPR signal (Fig. S5†).[54] Thus, the samples were activated at 423 K in vacuum and measured under Ar. The spectra of the activated samples exhibit a relatively sharp signal

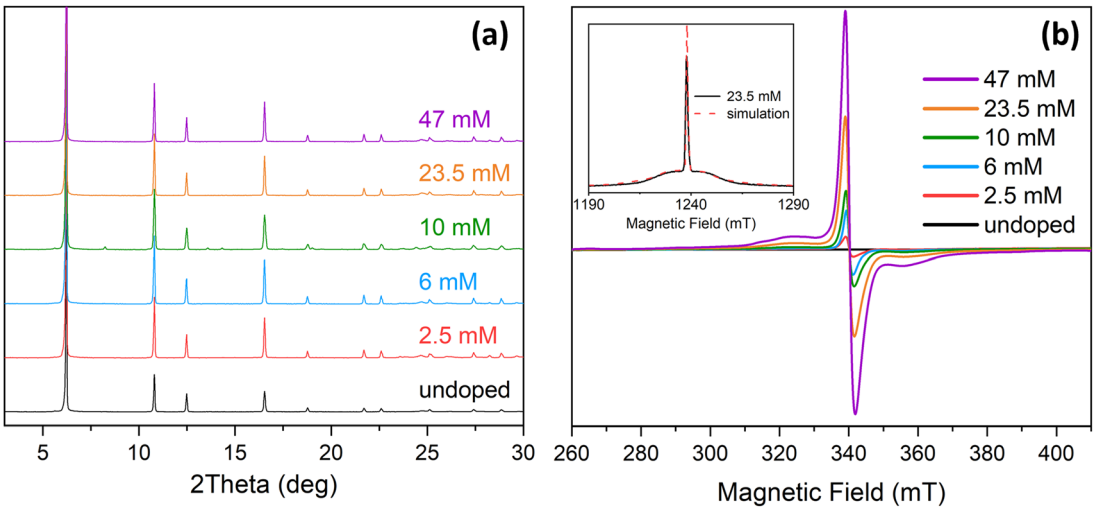


Fig. 1 (a) X-ray diffraction patterns acquired for undoped LaBTB (black) and Gd-doped LaBTB with 2.5 (red), 6 (blue), 10 (green), 23.5 (orange) and 47 mM (purple) Gd(III) concentration. Measurements were carried out under Ar atmosphere after activation of the samples at 423 K in vacuum. (b) CW-EPR spectra of the activated Gd-LaBTB samples with 2.5 (red), 6 (blue), 10 (green), 23.5 (orange) and 47 mM (purple) Gd(III) concentration measured on X-band at 100 K. Inset: the FSED spectrum of 23.5 mM Gd-LaBTB (black) acquired at Q-band at 100 K and a simulation (red) of the Gd(III) spectrum with $S = 7/2$, $g = 1.99$ and ZFS parameters of $D = 312$, $E = 0$ MHz with strains of 280 and 0 MHz, respectively.

at $g = 1.99$ confirming the presence of Gd(III) ions in all samples (Fig. 1b). The signal intensity grows with increasing Gd(III) loading, consistent with homogenous doping of the samples. The homogeneity of the Gd(III) distribution is also supported by a monotonic change in the nuclear relaxation time $T_1$ and the intensity of the NMR signal (see below). No change in the peak-to-peak width was observed as a function of Gd(III) concentration (Fig. S6†), likely due to the relatively low concentration of Gd(III) throughout the series of samples and/or dynamics in the MOFs which lead to averaging of the Gd(III)–Gd(III) dipolar interactions.[54]

To determine the EPR parameters of the Gd(III) ions, we recorded a field sweep echo-detected (FSED) EPR spectrum at 34.2 GHz (Q-band) at 100 K for the 23.5 mM Gd-LaBTB sample activated at 423 K. The spectrum was fitted using EASYSPIN[55] with a single-Gd species with electron spin $S = 7/2$, $g = 1.99$, and zero-field splitting (ZFS) parameters of $D = 312$, $E = 0$ MHz with strains of 280 and 0 MHz, respectively (Fig. 1b). Note that fitting was performed without considering motional averaging of the ZFS tensor (see below). The relatively low value of the ZFS parameter $D$ suggests that all Gd(III) ions in the MOF sample are in a close to symmetric environment.[56] These parameters were then used to simulate the EPR spectrum of Gd-LaBTB at 9.4 T and electron frequency of 263.5 GHz, corresponding to the conditions of the DNP NMR experiments (Fig. S7†).

### Solid-state NMR of Gd-LaBTB samples

LaBTB samples were investigated using conventional solid-state NMR spectroscopy. The $^1$H MAS NMR spectrum of undoped LaBTB, recorded at 100 K with 9 kHz spinning rate, exhibits one broad unresolved signal at *ca.* 7 ppm, characteristic for the aromatic protons of the BTB linker (see Fig. S8†).[53] At room temperature $^1$H MAS NMR measurements, performed at 60 kHz spinning rate, two signals could be resolved at 6–7 ppm, that can be assigned to protons of the central and side benzene rings of the BTB linkers (Fig. 2a).[53] Doping of LaBTB with Gd(III) does not lead to the appearance of additional $^1$H NMR signals, suggesting that the MOF structure remains unchanged (Fig. S8 and S9†).

$^{13}$C CPMAS NMR spectrum of the undoped LaBTB, recorded at 100 K with 9 kHz spinning rate, displays one resonance at 182.4 ppm and two sets of resonances - from 146 to 139 ppm and from 136 to 123 ppm – that are not fully resolved (Fig. 2b). These spectral regions are characteristic for carboxyl, substituted and non-substituted C–H aromatic carbon atoms, respectively.[57] Deconvolution of the spectrum revealed four signals in the substituted carbon region and six signals in the C–H carbon region. Each $BTB^{3-}$ moiety contains one type of carboxyl carbon, three substituted and three C–H aromatic carbon sites that are chemically non-equivalent. However the equivalency of the carboxy groups is removed in the LaBTB crystal structure with one carboxyl group of the linker chelating one lanthanum ion and two other carboxyl groups bridging between two adjacent La(III) (Fig. S10†).[49] This results in two, six and eight crystallographically non-equivalent carboxyl, substituted and C–H aromatic carbons, respectively. Some of the carbons likely have a very similar $^{13}$C chemical shift and are not resolved in the spectrum. As a result, only eleven resonances (1 + 4 + 6), instead of sixteen (2 + 6 + 8) expected from the crystal structure, are required to deconvolute the spectrum (Fig. 2b).

As in the $^1$H NMR, no new signals were observed in the $^{13}$C spectra of the Gd-doped samples, supporting the preservation of LaBTB structure (Fig. S11†). Note that while the presence of paramagnetic metal ions is known to significantly broaden and possibly shift the NMR resonances of nearby nuclei (*via* dipolar

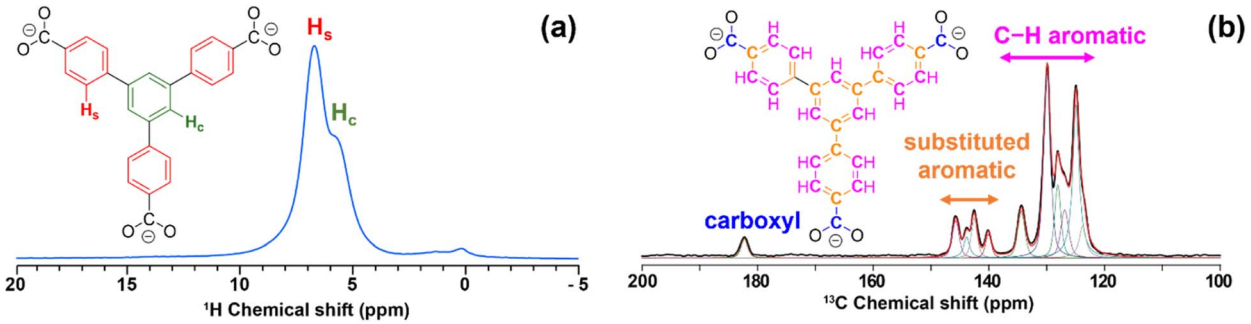


Fig. 2 (a) $^{1}$H MAS NMR spectrum of undoped LaBTB sample acquired at ambient temperature and 60 kHz MAS. Hydrogen atoms of the central benzene ring and side benzene rings of the BTB linker are highlighted in green and red, respectively. The signal at *ca.* 0 ppm is an impurity from the rotor. (b) $^{13}$C CPMAS NMR spectrum (black) of undoped LaBTB acquired at 100 K and 9 kHz MAS. The spectrum was deconvoluted in dmfit software[92] and the obtained fit is shown in red. Carboxyl, substituted and non-substituted C–H aromatic carbon atoms of the BTB linker are highlighted in blue, orange and magenta, respectively.

and Fermi contact interactions, respectively), these sites are not detected at low concentration of paramagnetic centers due to their fast nuclear $T_2$ relaxation (so-called paramagnetic quenching).[58] For $^{13}$C sites which are further away from the paramagnetic metal ions and are observed in the spectrum Gd doping results in decreased relaxation times and broadening.

### Nuclear relaxation in LaBTB at 100 K

One of the parameters that is important for the efficiency of MIDNP in increasing NMR sensitivity is the longitudinal relaxation times of the nuclei that are to be hyperpolarized: increase in the $T_1$ nuclear relaxation time is known to have a beneficial effect on the DNP enhancement.[59,60] Long $T_1$ is critical for polarizing nuclei that are further away from the paramagnetic metal ion, in particular for nuclei for which spin diffusion is negligible. Limited spin diffusion can be a result of weak dipolar couplings due to low gyromagnetic ratio, low natural abundance, and/or motional averaging of the dipolar couplings. In this case, polarization is transferred directly from the polarizing agent to all nuclei in the sample, and more distant nuclei require longer time to be polarized – a time limited by their intrinsic $T_1$ relaxation. Therefore, careful control over nuclear relaxation is key for increasing MIDNP performance.

DNP experiments are typically performed at 100 K which helps to slow down electron relaxation – another determinative parameter for DNP, and MIDNP in particular.[58,61] Typically, in MAS-DNP experiments samples are packed into NMR rotors, introduced inside a cold (*ca.* 100 K) DNP probe and are spun with a cold $N_2$ flow. Generally, the nuclear longitudinal relaxation time in solids is also expected to be longer at 100 K than at ambient temperature.[62] However, in the case of LaBTB we observed an unusual behavior of nuclear relaxation: while $T_1$ of $^{1}$H nuclei is only 0.2 s right after the sample is inserted inside the cold probe, over time $T_1(^{1}H)$ monotonically increases reaching a plateau after *ca.* 4 hours at a value of *ca.* 2 s (Fig. 3a). An increase of $T_1(^{1}H)$ with time was also observed for Gd-doped LaBTB samples (Fig. S12†).

We suggest two possible explanations for the surprisingly slow change in protons $T_1$: (1) the presence of trapped molecular $O_2$ in the pores of LaBTB, and (2) motion of the framework material. While the samples were activated in vacuum and packed into the rotor under inert atmosphere, some residual oxygen may be adsorbed or confined within the microporous structure. As $O_2$ is paramagnetic it is known to enhance nuclear relaxation.[63,64] Gradual changes in $T_1$ relaxation can then occur if spinning the sample with $N_2$ at 100 K leads to slow removal of $O_2$, resulting in an increase in $T_1$ with time.[63,64] We note that this effect should be irreversible: after reaching a plateau, $T_1$ should remain unchanged if the sample is warmed up under $N_2$ and cooled down back to 100 K. The second plausible explanation for the initially short $T_1(^{1}H)$ is the presence of motions in the LaBTB framework that are the source of nuclear relaxation. Indeed, the presence of molecular motions, such as rotation, flipping and small-angle librations of linkers is a known phenomenon for MOFs, even at temperatures lower than 100 K.[65–69] We can expect changes in the framework mobility from the instant the sample is inserted into the cold probe due to gradual cooling of the sample as well as replacement of the argon gas filling the pores with the cold nitrogen molecules. It is well known that MOFs have low thermal conductivity,[70–73] which would also depend on the gas filling the pores.[74] Thus the framework may require relatively long times to equilibrate at 100 K, including both the thermal motion and gas displacement in the pores, which would lead to partially or completely freezing the motions that cause fast nuclear relaxation. This would also result in a non-instantaneous growth of $T_1(^{1}H)$, assuming that the correlation time of the motions is longer than the inverse of the angular Larmor frequency (slow-motion regime). This effect is expected to be somewhat reversible if the sample is warmed up and then again inserted inside the cold probe.

To better understand the cause for the intriguing $T_1$ behavior in LaBTB samples, we performed a "freeze-thaw" procedure for the undoped LaBTB and determined its effect on $T_1(^{1}H)$. This procedure is proposed in the DNP literature as an efficient method to remove $O_2$ from both solvent-impregnated samples and solvent-free solid powders, such as polymers.[75,76] Indeed, the "freeze-thaw" process had a great impact on $T_1(^{1}H)$ (Fig. 3b).

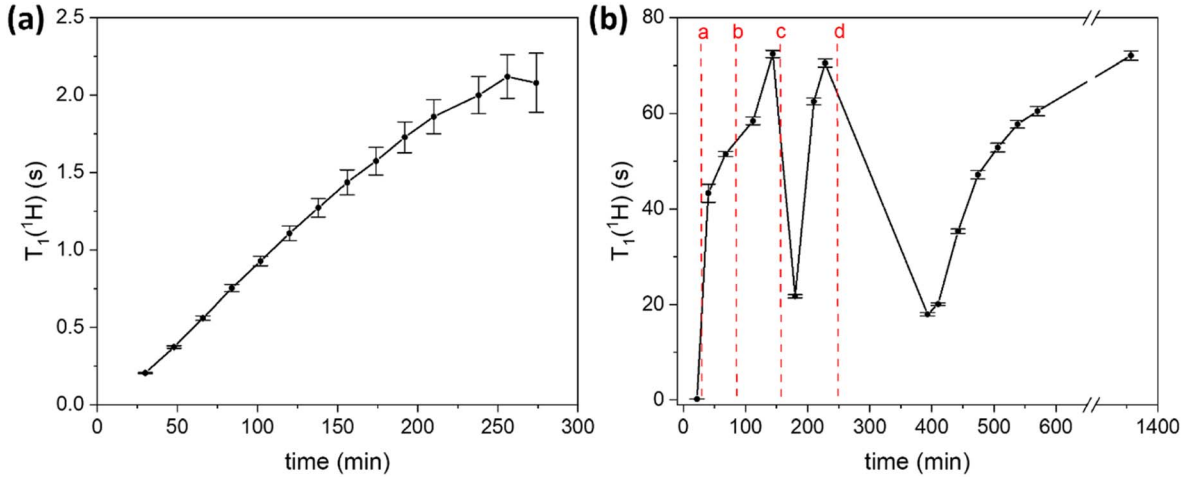


Fig. 3 (a) $^1$H relaxation time $T_1$ as a function of time from insertion of the undoped LaBTB sample into the cold (*ca.* 100 K) LT-DNP probe. (b) Effect of "freeze-thaw" cycles on $^1$H $T_1$ relaxation time of undoped LaBTB: (a) – 1st "freeze-thaw" cycle with 5 min thaw; (b) – 2nd "freeze-thaw" cycle with 5 min thaw; (c) – 3rd "freeze-thaw" cycle with 10 min thaw; (d) – 4th "freeze-thaw" cycle with 60 min thaw. $T_1(^1H)$ is plotted *vs.* time starting from the insertion of the sample into LT-DNP probe.

After the first "freeze-thaw" cycle (a), the nuclear relaxation time changed from 0.2 s to more than 40 s, growing further to >50 s with time. Another "freeze-thaw" cycle (b) led to even higher $T_1(^1H)$ value approaching 72 s after 30 min. When the "freeze-thaw" step was repeated the third time (c), instead of growing further, $T_1(^1H)$ value dropped down to 22 s but after 1 h at 100 K again increased up to 71 s. To verify that this is reproducible, another "freeze-thaw" cycle with a long thaw step was carried out (d): indeed, $T_1(^1H)$ first decreased to 18 s and over several hours grew back to >60 s. These results can be rationalized as follows: The first, and probably also the second, "freeze-thaw" cycles led to $O_2$ removal from the sample which resulted in longer nuclear relaxation. The subsequent cycles did not lead to increase of $T_1(^1H)$, likely because there was no $O_2$ left after the first two cycles. The observed drop in $T_1(^1H)$ could be explained by the sample warming up at the bottom of the probe leading to (i) increase in the thermal motions (*vide infra*) that enhance relaxation as well as (ii) relatively fast desorption of part of the argon/nitrogen gas filling the pores at non-cryogenic temperatures.[77] Over time these motions slow down again (gradually due to the limited thermal conductivity and/or adsorption process of cold nitrogen gas), resulting in the subsequent growth in $T_1(^1H)$. Thus, our results demonstrate that both the presence of $O_2$ and the slow freezing of motions are very likely the reasons for the initially short $T_1(^1H)$ and its temporal change in LaBTB sample. Note that without "freeze-thaw" cycles $T_1(^1H)$ reached a value of only 2 s (Fig. 3a) which is much shorter than after the "freeze-thaw" experiment. We believe that $O_2$ cannot be completely removed by flushing the sample with $N_2$ at 100 K. To verify this, a quantitative measurement of the amount of $O_2$ would be required inside the DNP probe, which is currently impossible.

To further confirm that the temporal changes in $T_1(^1H)$ in oxygen-free (Gd)-LaBTB samples originate from the non-instantaneous freezing of motions, we took advantage of the high sensitivity of the ZFS anisotropy of the Gd(III) dopants to the motions of the framework.[78] The 6 mM Gd-LaBTB sample, sealed in a capillary under Ar, was inserted into the EPR resonator pre-cooled to 100 K, and the EPR spectra were recorded every 10 min over a course of 2.5 h. The Gd(III) EPR signal clearly changes with time: the central transition resonance monotonously decreases in intensity and significantly broadens (Fig. 4), while the centres of the two Gd(III) satellite transitions (unresolved due to the strain in ZFS parameter $D$, see Fig. S7†) shift away from the centre (Fig. S13†). These observations indicate that the Gd(III) ZFS anisotropy increases with time at 100 K,

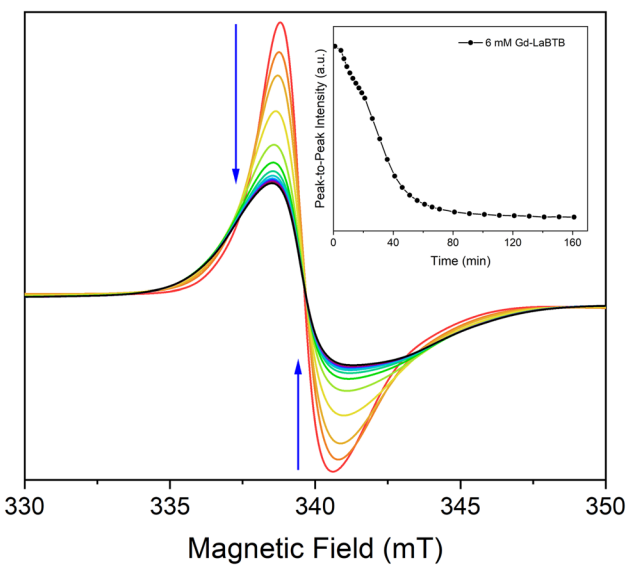


Fig. 4 CW-EPR spectra of the 6 mM Gd-LaBTB sample recorded every 10 min on a X-band spectrometer at 100 K. Blue arrows indicate the changes with time. Inset: the temporal change of the peak-to-peak intensity of the Gd(III)central transition. The sample was activated at 423 K in vacuum and measured under Ar.

further supporting the temporal changes in the MOF's dynamics. It is worth noting that the sensitivity of the ZFS anisotropy to the motional freezing at 100 K suggests that the timescale of these motions should be of the order of the inverse of the ZFS parameter $D$ which is $10^8$–$10^9$ Hz. Thus, the correlation time of these motions is *ca.* $10^{-8}$–$10^{-9}$ s, close to the inverse of the $^1$H nuclear Larmor frequency, hence being an efficient source for the nuclear relaxation. Such fast molecular motions were previously observed for MOF-based materials, even at temperatures lower than 100 K.[65,67]

For obtaining consistent results in MIDNP experiments on Gd-LaBTB the nuclear relaxation time should be constant at 100 K. In the following experiments, samples were either kept inside the DNP probe until $T_1(^1H)$ was stable or were subjected to several "freeze-thaw" cycles until no further increase in $T_1(^1H)$ was observed. The stabilized $T_1(^1H)$ was significantly shorter with the first approach, with more significant difference between the two approaches observed for samples with low Gd(III) concentration (Fig. S14†). The effect of the stabilization procedure (*i.e.* the process of stabilizing the MOF relaxation) on the DNP efficiency will be discussed below.

## DNP field-sweep profiles

Next, we assessed the performance of Gd(III) as a polarizing agent for MIDNP. To find an optimal position of the magnetic field, which provides the maximal enhancement of NMR signal, we acquired field-sweep profiles for $^1$H and $^{13}$C nuclei.[79,80] This is done by measuring the signal intensity of the corresponding nucleus as a function of the magnetic field during microwave irradiation.

Field-sweep profiles for Gd-LaBTB sample with the target Gd(III) concentration of 6 mM are plotted on Fig. 5. Measurements were done after the sample was kept in the cold probe until a constant $T_1(^1H)$ was observed without "freeze-thaw" cycles. The sweep profiles were collected for a material containing lanthanum formate impurities (see Fig. S4†). In $^{13}$C spectra, the MOF and the formate resonances were well-resolved, allowing us to selectively integrate the MOF signals. In contrast, in $^1$H NMR spectra, the signals of the two phases overlapped at 100 K, and the obtained $^1$H field-sweep profile has contributions from both phases. Nevertheless, comparison of the $^{13}$C field-sweep profiles for the MOF and the $La(HCO_2)_3$ phase shows that both profiles exhibit a negative and a positive lobe, and the maxima/minima of the lobes are at the same field position for both phases (Fig. S15†). This implies that the optimal position of the field in the reported $^1$H field-sweep profile (Fig. 5) corresponds to the optimal field position for $^1$H DNP in the MOF phase – which is the information we aimed to obtain from the sweep.

The $^{13}$C field-sweep profile has distinct positive and negative lobes separated by *ca.* 7.2 mT (or 202 MHz) that is twice the nuclear Larmor frequency for $^{13}$C nuclei at 9.4 T. The center between the two lobes is at 9.457 T – corresponding to $g = 1.99$, matching perfectly the position of the Gd(III) EPR line. Therefore, the $^{13}$C field-sweep profile suggests that Gd(III) dopants transfer polarization to $^{13}$C nuclei *via* the solid effect mechanism.[58] As can be seen in Fig. 5, the positive and negative

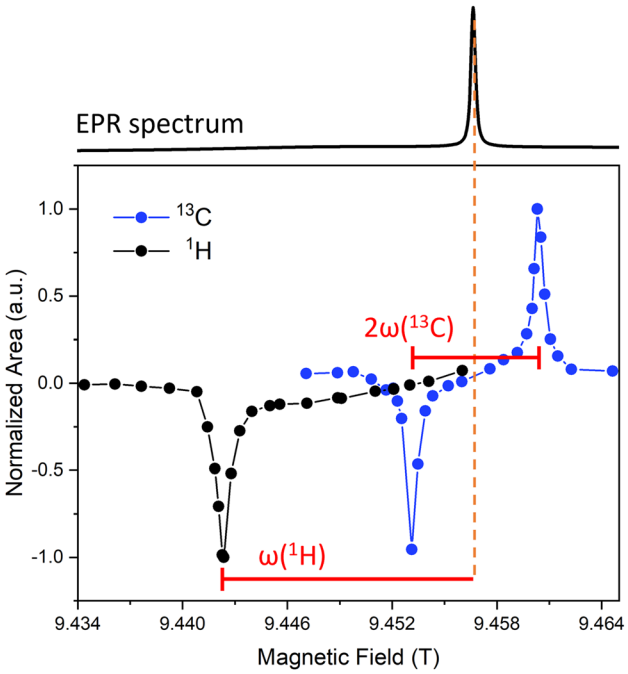


Fig. 5 DNP field-sweep profiles acquired for $^{13}$C (blue) and $^1$H (black) nuclei in Gd-LaBTB sample with the target Gd(III) concentration of 6 mM. The sample was stabilized until a constant $T_1(^1H)$ was measured without "freeze-thaw" cycles. Spectra were recorded with polarization times of 40 and 4.5 s for $^{13}$C and $^1$H, respectively. At the top, the simulated EPR spectrum of Gd-LaBTB at 9.4 T and electron frequency of 263.5 GHz is shown.

maxima have nearly the same magnitude, thus any of the two corresponding field positions can be chosen to obtain maximal enhancement for $^{13}$C nuclei. Within the available range of the magnetic field we could only detect the negative lobe (at 9.442 T) in the $^1$H field-sweep profile. The $^1$H negative lobe is 15 mT (or 420 MHz) away from the center of the $^{13}$C sweep profile, which roughly corresponds to the nuclear Larmor frequency for $^1$H. This suggests that the solid effect mechanism is also dominant for $^1$H. As the positive lobe expected at 9.472 T cannot be reached on our spectrometer, $^1$H signal enhancement was determined at the field corresponding to the negative lobe.

## Effect of relaxation on the DNP efficiency

We now turn to evaluate how the increase in $T_1$ relaxation time due to either $O_2$ removal or freezing of motions affects the DNP enhancement in Gd-LaBTB. The enhancement ($\varepsilon_{on/off}$), defined as the ratio between the integrated NMR signal recorded with and without microwave irradiation, was determined without and with "freeze-thaw" cycles at steady state conditions (acquired with a relaxation delay $>5T_1$ corresponding to the instantaneous $T_1$ value). As the measurements were performed for $^1$H nuclei (chosen because of their short acquisition time) at the negative lobe in the field-sweep profile an inverted signal is expected with microwaves if DNP is efficient.[58] Following insertion of the 10 mM Gd-LaBTB into the cold DNP probe, the value of $\varepsilon_{on/off}$ for $^1$H was 0.6 ± 0.1 (Fig. 6a). The DNP effect was lower than the $^1$H signal at thermal equilibrium, hence

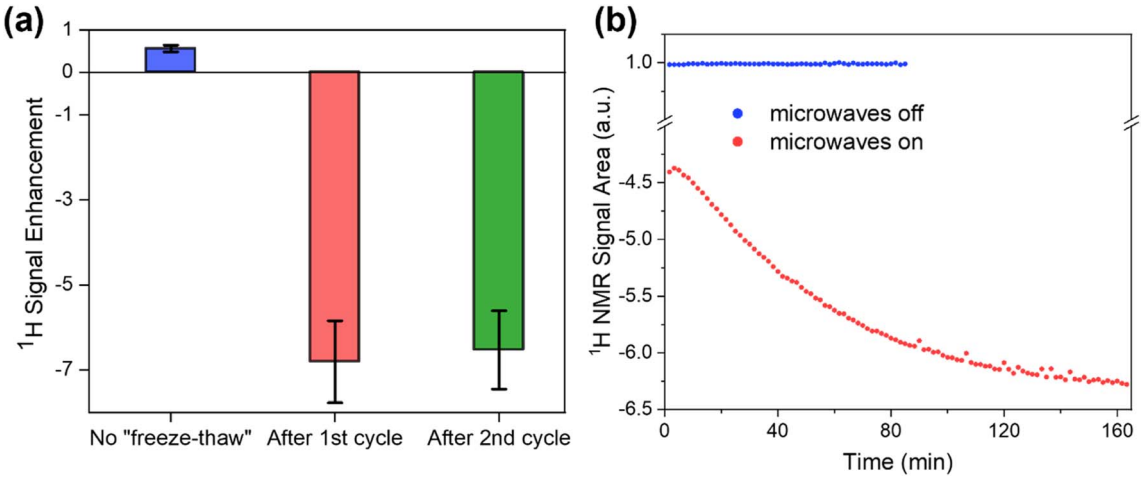


Fig. 6 (a) $^1$H signal enhancement ($\varepsilon_{on/off}$) measured for 10 mM Gd-LaLOF at 100 K and the magnetic field corresponding to the negative lobe of the $^1$H field-sweep profile: before "freeze-thaw" cycles (blue), after subjecting the sample to one (red) or two subsequent (green) "freeze-thaw" cycles with 5 min thaw each. All spectra were recorded with >5$T_1$ delay between signal saturation and the 90° excitation pulse. $T_{bu}$ values were slightly shorter than corresponding $T_1$; (b) Integrated area of the $^1$H NMR signal acquired for 2.5 mM Gd-LaLOF at 100 K at the negative lobe of the $^1$H field-sweep profile with microwaves off (blue) and on (red). The sample was subjected to two 5 min "freeze-thaw" cycles until $T_1$($^1$H) was stabilized, thawed for 30 min, and then inserted back into the DNP probe stator kept at 100 K. From that point, $^1$H spectra were acquired every 1.7 min. The microwave-on signal area was normalized by the microwave-off signal area, and its negative sign indicates that the microwave-on signal is inverted with respect to the microwave-off signal. The microwave-off experiment was stopped after 80 min since there was no change over the time.

no inversion of the microwave-on signal is observed but only a partial decrease in intensity. However, after the first "freeze-thaw" cycle, the $^1$H resonance was inverted with an $\varepsilon_{on/off}$ of $-7 \pm 1$ (Fig. 6a). This was accompanied by an increase in $T_1$($^1$H) from 0.3 s to >8 s. An additional "freeze-thaw" cycle did not change the $T_1$($^1$H), and accordingly, $\varepsilon_{on/off}$ remained unchanged within error. Therefore, the presence of $O_2$ in the Gd-LaBTB samples has a significant negative impact on the MIDNP efficiency. We then let the $O_2$-free sample thaw for 30 min under $N_2$ flow (at the base of the DNP probe) and cooled it again. As was discussed above, this leads to a decrease in $T_1$($^1$H) with a subsequent monotonous increase over a few hours up to the $T_1$($^1$H) value obtained after removing $O_2$ (see Fig. 3b). This observation was rationalized as an activation of motions and desorption of guest gas molecules by the higher temperature at the base of the DNP probe which leads to increased relaxation,[62] followed by slowing down of the MOF dynamics at 100 K. During the time of $T_1$($^1$H) growth, the microwave-on $^1$H NMR signal (inverted with respect to microwave-off signal) was increasing in intensity, approaching a plateau after >2.5 h (Fig. 6b and S16†). In the control experiment, the microwave-off $^1$H NMR signal intensity showed no time-dependence when it was acquired continuously by adjusting the relaxation delay to 5$T_1$ (Fig. 6b). Thus, we conclude that $^1$H enhancement is sensitive to the changes in relaxation caused by motion. To summarize, the highest DNP enhancement can be achieved by $O_2$ removal *via* the "freeze-thaw" procedure followed by a subsequent prolonged freezing of motions until $T_1$($^1$H) reaches its maximum value.

### Effect of Gd(III) concentration on the DNP performance

Next, we investigated how MIDNP efficiency in Gd-LaBTB depends on the concentration of the Gd(III) dopant. As mentioned above, the relaxation of $^1$H is significantly prolonged by removing $O_2$ *via* the "freeze-thaw" procedure (Fig. S14†), and this results in the substantial improvement of the DNP enhancement of the $^1$H NMR signal. Moreover, when the paramagnetic metal ions (in a small quantity used for MIDNP) are the main source of nuclear relaxation, higher concentration of the paramagnetic dopant leads to shorter $T_1$. This effect is known as paramagnetic relaxation enhancement (PRE).[81] However, without "purposely" deoxygenating the Gd-LaBTB samples, a random dependence of the stabilized $T_1$($^1$H) on Gd(III) concentration was found. This indicates that $O_2$ amount varies among samples and has an impact on relaxation. In contrast, after the "freeze-thaw" cycles, $T_1$($^1$H) monotonously decreases with Gd(III) concentration, suggesting that Gd(III) ions are the main source of relaxation (Fig. S14†). Therefore, the effect of Gd(III) concentration on MIDNP performance can only be investigated after removing $O_2$.

We found that for the $^1$H nuclei $\varepsilon_{on/off}$ acquired at steady state (polarization time >5$T_{bu}$, with $T_{bu}$ the polarization build up time constant) depends on the Gd(III) concentration. The highest enhancement for $^1$H is $10 \pm 1$ fold in the sample with the lowest Gd(III) content, 2.5 mM Gd-LaBTB, and it decreases with higher concentrations of the Gd(III) dopant, being $4.4 \pm 0.6$ fold for 47 mM Gd-LaBTB (see Fig. S17†). To have a better assessment of the sensitivity gain, in addition to $\varepsilon_{on/off}$ we must take into account effects of paramagnetic quenching by the Gd(III) ions[58,82] and the change in the experimental time due to enhanced relaxation caused by Gd(III) doping.[83] Paramagnetic

quenching was estimated as the ratio (in %) between the $^1$H NMR signal of Gd(III)-doped and undoped LaBTB samples acquired with no microwave irradiation, detected with a relaxation delay of $5T_1$. For 2.5 mM Gd-LaBTB there was no change in the integrated signal intensity with respect to the undoped LaBTB (Fig. S18†). However, with higher concentration a vast decrease in the $^1$H signal was observed, with only 32 ± 3% of the signal of the undoped material left in the 47 mM Gd-LaBTB sample. Additionally, as the dopant concentration increased, the $T_1$ value decreased (*vide infra*), and so did the $T_{bu}$. For the undoped LaBTB, $T_1(^1H)$ is 86 ± 2 s, while for the highest Gd(III) concentration of 47 mM, $T_{bu}(^1H)$ is only 1.00 ± 0.02 s (Fig. S19†). The normalized enhancement ($\varepsilon_x^{norm}$) corrected for the paramagnetic quenching ($\Theta_x$) and the relaxation enhancement was calculated as $\varepsilon_x^{norm} = (\varepsilon_{on/off})_x \times \Theta_x \times [(T_1)_{undoped}/(T_{bu})_x]^{1/2}$,[64,83] where $(T_1)_{undoped}$ is the relaxation time for the undoped LaBTB, measured with microwaves off and $(T_{bu})_x$ is the build-up time for a given sample. Up to 10 mM, $\varepsilon^{norm}$ was 20 ± 2 fold, while for 47 mM its value dropped to 13 ± 1 fold (Fig. S17†). Thus, for $^1$H nuclei, the sensitivity is higher for lower Gd(III) concentrations.

While $^1$H NMR spectra with a good signal-to-noise ratio can be collected within a couple of minutes for a MOF sample, $^{13}$C nuclei are more challenging due to their low natural abundance (1%) and lower intrinsic sensitivity. The $^{13}$C field-sweep profile indicates that polarization can be transferred from Gd(III) sites directly to $^{13}$C nuclei *via* solid effect. We thus determined the enhancement factors $\varepsilon_{on/off}$ that can be achieved for $^{13}$C nuclei and investigated how $\varepsilon_{on/off}$ is changing with Gd(III) concentration. Note that as for $^1$H, relaxation (and build-up) times of $^{13}$C nuclei became several folds longer after the Gd-LaBTB samples were subjected to "freeze-thaw" cycles (Fig. S20†). Therefore, $\varepsilon_{on/off}$ factors were compared for deoxygenated samples.

The $^{13}$C MAS NMR spectra of the 10 mM Gd-LaBTB sample, recorded with and without microwaves at the magnetic field corresponding to the negative lobe of $^{13}$C, are shown in Fig. 7a. For illustration purposes, the microwave-on spectrum is inverted. Signals of carboxyl, substituted and C–H aromatic carbons of the BTB linker are notably more intense with microwaves, hence all carbons of the MOF linker are hyperpolarized. For each Gd(III) concentration, we deconvoluted the microwave-off and microwave-on spectra, both recorded with a $5T_{bu}$ delay, and integrated each signal separately to estimate $\varepsilon_{on/off}$ for different carbon species (see Table S2†). An average $\varepsilon_{on/off}$ value over all signals *vs.* Gd(III) concentration is plotted in Fig. 7b. Within the range of concentrations investigated here $\varepsilon_{on/off}$ is *ca.* 30 and is independent of the concentration within error. This $\varepsilon_{on/off}$ translates to *ca.* 900-fold saving in experimental time.

Although $\varepsilon_{on/off}$ was found to be very similar across the samples, with increasing Gd(III) concentration, the intensity of all $^{13}$C NMR signals (with and without microwaves) decreases due to paramagnetic quenching (Fig. S11†), similarly to the $^1$H nuclei. Note that due to the very long $^{13}$C relaxation time in the undoped sample, we were not able to record a quantitative $^{13}$C MAS NMR spectrum of LaBTB and determine the quenching factor for $^{13}$C NMR signals. Nevertheless, we made an estimation of the relative quenching for Gd-doped samples: $\Theta_x^{rel} = (A_x/A_{2.5\ mM}) \times 100\%$, where $A_x$ is the total area of the microwave-off $^{13}$C spectrum for the given concentration and $A_{2.5\ mM}$ is the total area for the 2.5 mM Gd-LaBTB. Up to 10 mM, the integrated signal intensity is the same within the error, but with a higher amount of paramagnetic dopant a notable decrease down to 66 ± 11% for 47 mM is found (Fig. S21†). Considering the different quenching across the samples as well as a significant decrease in $T_1$ and $T_{bu}$ with Gd(III) concentration (Fig. S20†), we normalized the enhancement factors relative to the 2.5 mM sample: $\varepsilon_x^{rel} = (\varepsilon_{on/off})_x \times \Theta_x^{rel} \times [(T_{bu})_{2.5\ mM}/(T_{bu})_x]^{1/2}$, where $\Theta_x^{rel}$ is a relative quenching factor for a given sample as defined above and $(T_{bu})_{2.5\ mM}$ the build-up time for 2.5 mM sample. $\varepsilon^{rel}$ grows monotonously with Gd(III) concentration, being >3 times higher for 47 mM sample compared to 2.5 mM (Fig. 7b). Therefore, among the samples studied in this work, the 47 mM Gd-LaBTB

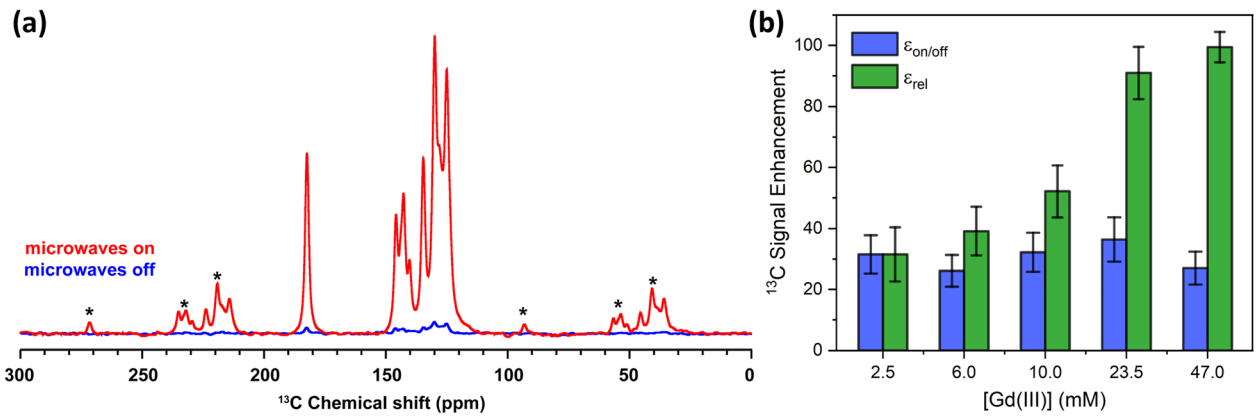


Fig. 7 (a) $^{13}$C MAS NMR spectra acquired for 10 mM Gd-LaBTB at 100 K with (red) or without (blue) microwaves at the optimal field position (negative lobe in the $^{13}$C field-sweep profile shown in Fig. 5). Asterisks indicate spinning side bands. (b) Enhancement factors for $^{13}$C nuclei as a function of Gd(III) concentration in Gd-LaBTB. $\varepsilon_{on/off}$ (blue) is determined as the ratio between integrated microwave-on and microwave-off signals at steady-state conditions ($5T_{bu}$). $\varepsilon_{rel}$ (green) is the enhancement $\varepsilon_{on/off}$ normalized by the paramagnetic quenching relative to 2.5 mM Gd-LaLOF (see Fig. S21†) and the change in the build-time $T_{bu}(^{13}C)$ with respect to the $T_{bu}(^{13}C)$ of 2.5 mM Gd-LaBTB (Fig. S20†). All samples were subjected to two 5 minutes long "freeze-thaw" cycles until stabilizing $T_1(^1H)$.

provides the highest sensitivity gain for $^{13}$C signals, when taking into account the effects caused by Gd(III) doping.

The above results demonstrate different dependence of the signal enhancement on Gd(III) concentration for $^{1}$H and $^{13}$C nuclei: while $\varepsilon_{on/off}(^{1}H)$ decreases with Gd(III) concentration, $\varepsilon_{on/off}(^{13}C)$ remains constant in the range of Gd(III) concentrations investigated here. This difference may originate from a combination of factors: (1) much shorter intrinsic $T_1$ relaxation time for $^{1}$H with respect to $T_1(^{13}C)$; (2) more severe quenching of the $^{1}$H signal at a given concentration of Gd(III) due to the stronger $^{1}$H-electron dipolar couplings at a given distance;[81] and (3) the contribution of spin diffusion to the polarization transfer for $^{1}$H nuclei *vs.* nearly pure direct polarization for the low abundance $^{13}$C nuclei in the Gd-LaBTB samples.[84] Indeed, for the oxygen-free undoped LaBTB sample, $T_1(^{1}H)$ was measured to be $86 \pm 2$ s (Fig. S14†), while $T_1(^{13}C)$ is longer than 2250 s (the value obtained for the lowest concentration Gd-LaBTB sample, see Fig. S20†). The long intrinsic $T_1(^{13}C)$ in LaBTB ensures that upon doping the relaxation of $^{13}$C is most likely dominated by PRE. In this scenario, the MIDNP efficiency is distance-independent,[61] and even nuclei that are far from Gd(III) ions will be hyperpolarized directly from the dopants.[85] Another indication for the dominance of direct polarization transfer for $^{13}$C nuclei over spin-diffusion is the $^{13}$C build-up curves which can be described by a stretched exponential function (with stretching factor <1, see Fig. S20†). Such behavior is typically a result of the contribution from distribution of distances to the paramagnetic center, for all Gd(III) concentrations. The distant-independent MIDNP efficiency results in $\varepsilon_{on/off}$ being independent of the Gd(III) concentration, under the assumption that increasing the concentration does not lead to significant change in electron relaxation times.[61] Indeed the experimentally observed $\varepsilon_{on/off}(^{13}C)$ are nearly constant within the concentration range studied (2.5 to 47 mM).

In contrast, $^{1}$H nuclei exhibit much shorter intrinsic relaxation times which limit the distance covered by direct polarization from Gd(III) (for an intrinsic $T_1$ of 80 s direct polarization is efficient up to about 0.7 nm from the metal ion).[58] Furthermore, for $^{1}$H nuclei polarization transfer by spin-diffusion is likely very efficient, as indicated by the nearly mono-exponential-growth observed for the build-up curves (with stretching factor close to 1, see Fig. S14 and Table S4†). While with increasing Gd concentration there are more nuclei that can be polarized directly, it is likely that these nuclei are not contributing directly to the signal as they are found within the quenching sphere and it is unknown to what extent they contribute to the spin diffusion process. The interplay between the polarization transfer mechanisms, directly from metal ions *vs.* spin diffusion mediated polarization, can result in an overall lower enhancement with increasing dopant concentration.

It is worth noting that the removal of $O_2$ *via* "freeze-thaw" cycles led to a significant improvement in the MIDNP performance for $^{13}$C nuclei across all Gd-LaBTB samples (see Fig. S22†). While $\varepsilon_{on/off}$ was $30 \pm 5$ after $O_2$ was removed, in the presence of oxygen $\varepsilon_{on/off}$ was *ca.* 3-times lower (*ca.* 10-fold enhancement). Thus, $O_2$ trapped in the pores of MOF has a strong negative impact on the MIDNP efficiency for $^{13}$C nuclei, in line with the results for $^{1}$H. A higher $\varepsilon_{on/off}(^{13}C)$ of $19 \pm 4$ was found for oxygen-containing 6 mM Gd-LaBTB, which deviates from the average $\varepsilon_{on/off}$ across the samples. This is most likely associated with the lower amount of $O_2$ present in the sample, the latter being in line with the longer $T_1(^{1}H)$ for this sample in comparison with the samples containing less Gd(III). (Fig. S14†).

Overall, the optimal enhancement factor obtained in this work, namely $\varepsilon_{on/off}(^{13}C)$ of $36 \pm 7$ for 23.5 mM Gd-LaLOF, is moderate in comparison with those previously reported for MIDNP in frozen solution[86,87] and in nonporous solids.[48,88,89] For instance, $\varepsilon_{on/off}(^{13}C)$ of $120 \pm 20$ (4.7% of the theoretical $\varepsilon_{on/off}$) was achieved for a 5 mM solution of [Gd(tpatcn)] complex in glycerol-water mixture. In solids, an optimal $\varepsilon_{on/off}(^{29}Si)$ of $110 \pm 20$ (3.4% of $\varepsilon_{on/off,theor}$) was found for 19 mM Gd-doped $Li_2CaSiO_4$; even higher $\varepsilon_{on/off}(^{89}Y)$ of 193 (1.4% of $\varepsilon_{on/off,theor}$) was observed for 40 mM Gd-doped Y–$CeO_2$; and finally for 4.2 mM Gd-doped $CeO_2$, an impressive $\varepsilon_{on/off}(^{17}O)$ of $652 \pm 5$ was obtained, reaching 13.4% of the theoretical enhancement. As was mentioned earlier, the efficiency of MIDNP is strongly affected by the electron relaxation properties of the polarizing agent, with higher product of longitudinal and transverse electron relaxation times ($T_{1e} \times T_{2e}$) leading to more efficient saturation of the DNP-relevant transitions and higher DNP enhancements.[58] $T_{1e}$ and $T_{2e}$ were measured for 23.5 mM Gd-LaLOF at Q-band (~1.2 T) at 100 K and their product is $T_{1e} \times T_{2e} = 0.24 \times 0.11 = 0.026\ \mu s^2$. For comparison, $T_{1e} \times T_{2e}$ of [Gd(tpatcn)] in a frozen solution was reported to be 0.22 $\mu s^2$ at 100 K on a W-band (~3.4 T).[86] That is one order of magnitude higher than in our Gd-doped LaBTB system. We have also determined $T_{1e} \times T_{2e}$ products for 19 mM Gd–$Li_2CaSiO_4$ and 40 mM Gd-Y-$CeO_2$ at the same conditions as for Gd-LaBTB and found that for 23.5 mM Gd-LaLOF the product is 5 times smaller than for 19 mM Gd–$Li_2CaSiO_4$ (0.086 $\mu s^2$) and 13 times smaller than for 40 mM Gd-Y-$CeO_2$ (0.344 $\mu s^2$). Therefore, the obtained moderate enhancement factors obtained for Gd-LaBTB are likely a consequence of the relatively fast electron relaxation. Further optimization of the MIDNP efficacy for MOFs should thus include the design of the system with longer electron relaxation, *e.g.* by performing the MIDNP experiments at temperatures lower than 100 K.

### DNP NMR of guest molecules in Gd-LaBTB

Having identified the optimal conditions for MIDNP in the Gd-LaBTB system, we sought to explore the applicability of this tool in elucidating host–guest interactions. To this end, we introduced ethylene glycol (EG) into the MOF pores. This was achieved through incipient wetness impregnation of an activated MOF sample with a THF solution of EG, followed by the subsequent solvent removal under vacuum. Attenuated total reflection infrared (ATR IR) spectroscopy revealed the appearance of IR bands at 2947–2870 $cm^{-1}$ (stretching $\nu_{CH}$ vibrations), 1450–1400 $cm^{-1}$ (bending $\delta_{CH}$ and $\delta_{COH}$ vibrations) and 1080–1030 $cm^{-1}$ (stretching $\nu_{CO}$ vibrations) regions, indicating a successful loading of the EG molecules into the Gd-LaBTB (Fig. S24†). The presence of additional bands at 2975 $cm^{-1}$ and 908 $cm^{-1}$ suggests that THF is not completely removed under vacuum, as was further supported by solid-state NMR

measurements (see below). No changes in the X-ray diffraction pattern were observed upon EG loading into the Gd-LaBTB sample, implying that the MOF crystal structure was preserved (Fig. S25†). Nevertheless, the presence of the guest molecules in the MOF affects the EPR signal of Gd(III), suggesting interactions between EG (and/or THF) with the metal ions in the MOF (Fig. S26†).

The introduction of EG/THF resulted in appearance of new resonances in the $^{13}$C NMR spectra of Gd-LaBTB (Fig. S27†). A signal at *ca.* 65 ppm has been assigned to the methylene ($CH_2$) group of EG, whereas signals at *ca.* 70 and 28 ppm can be attributed to the –$CH_2CH_2O$– and –$CH_2CH_2O$– moieties, respectively, originating from residual THF solvent. Interestingly, additional resonances emerge within spectral regions characteristic of the carboxyl and aromatic carbons of the MOF. These resonances may be a result of the interactions between EG (and/or THF) and the framework, leading to alterations in the local environment of the MOF linkers and changes in their $^{13}$C chemical shift.[90,91] This interpretation is supported by correlations observed in a $^{1}$H–$^{13}$C HETCOR spectrum, wherein $^{13}$C NMR signals of the MOF and EG (as well as MOF and THF) correlate with the same $^{1}$H resonances (Fig. S28†). These results suggest a successful incorporation of guest molecules into the Gd-LaBTB structure while preserving its crystalline integrity.

We then investigated whether polarization could be transferred from the Gd(III) dopant in the MOF to the guest molecules within its structure. To this end, we recorded $^{13}$C MAS NMR spectra of the EG-loaded Gd-LaBTB sample with and without microwaves, at the magnetic field position corresponding to the negative lobe in the $^{13}$C field-sweep profile (Fig. 8). At this field position, it is expected that the signals of the hyperpolarized $^{13}$C nuclei in the microwave-on spectrum will be inverted with respect to the corresponding signals in the microwave-off spectrum. As illustrated in Fig. 8, apart from the MOF signals, the signal attributed to EG is inverted upon microwave irradiation. This observation suggests that the MIDNP approach can be employed to hyperpolarize guest molecules. Furthermore, the MOF signals emerging in the $^{13}$C NMR spectrum following EG/THF loading, are also inverted, indicating the potential of MIDNP for probing host–guest interactions in MOFs. Another intriguing observation is that the signals originated from the residual THF solvent maintain their phase in the microwave-on spectrum. This implies that, unlike EG, THF is not hyperpolarized by the Gd(III) ions. Such difference in the DNP response might be a result of the higher mobility of the THF molecules within the host structure, which impedes the transfer of polarization. The negligible absolute enhancement of the EG signal, together with the reduced enhancement factors for the MOF signals ($\varepsilon_{on/off}$ of *ca.* 10 *vs.* 30 in the guest-free Gd-LaBTB) are likely also a consequence of the high mobility of the guest molecules within the MOF. The effect of the strength of the host–guest interactions on the DNP efficiency will be a subject of future investigations.

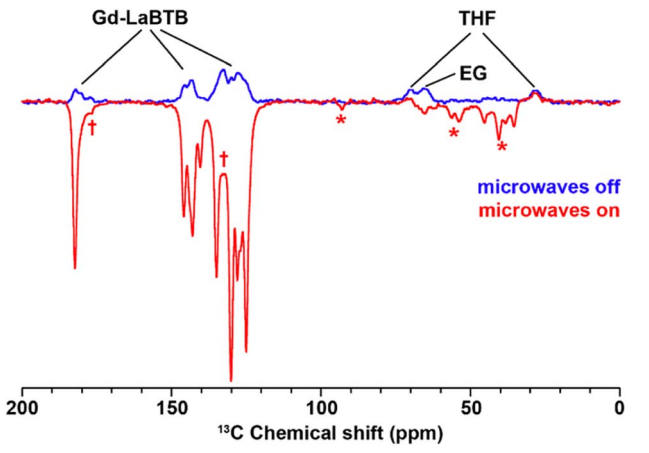


Fig. 8 $^{13}$C MAS NMR spectra acquired for 23.5 mM Gd-LaBTB loaded with EG/THF at 100 K with (red) or without (blue) microwaves at the optimal field position (negative lobe in the $^{13}$C field-sweep profile shown in Fig. 5). Asterisks indicate spinning side bands. Daggers indicate new MOF resonances appearing upon introduction of EG/THF.

## Conclusions

We have demonstrated that Gd(III) ions doped into a La-based metal–organic framework LaBTB can be successfully exploited as polarizing agents for endogenous metal-ion DNP. The polarization is transferred from the Gd(III) ions to the nuclei of the LaBTB linkers *via* solid effect. Signal enhancement factors of 10 and 36 were obtained for $^{1}$H and $^{13}$C nuclei, respectively, in Gd-LaBTB which translate to 2 and 3 orders of magnitude saving in experimental time, respectively. In contrast to conventional exogenous DNP, our approach provides sensitivity gains without the need to impregnate the MOF with the solution of organic radicals, thus it is not destructive and leaves the pores empty for the adsorption of guests. We were able to show that ethylene glycol, introduced into the MOF as a guest molecule, is also polarized from the Gd(III) ions, suggesting that our metal-ion DNP approach has potential for studying host–guest interactions in MOFs. We have also found that MIDNP efficiency in Gd-doped LaBTB is strongly influenced by the molecular oxygen present in the pores. When the MOF was subjected to "freeze-thaw" cycles, that is an established approach for removing $O_2$ from samples measured at low temperature, the enhancement of both $^{1}$H and $^{13}$C nuclei drastically increased. Moreover, our results suggest that significant dynamics is present in LaBTB which has a negative effect on MIDNP. We found that the framework mobility requires up to several hours to slow down at 100 K, an essential step for maximizing the DNP efficacy in the studied MOF. During this time, nuclear relaxation times are monotonously increasing and so does the DNP enhancement. The presence of oxygen and the effect of motions are likely a general property of MOF materials and should be considered if one wishes to achieve the best MIDNP performance in this important class of materials.

## Data availability

Data is available upon request.

## Author contributions

I. B. M.: synthesis and characterization of materials, DNP experiments, EPR measurements at X-band, data analysis, writing – original draft. Y. F.: assistance and guidance with X-ray diffraction and X-ray fluorescence analysis of materials; R. C.: assistance and guidance with EPR measurements at Q-band; X. L.: $CO_2$ adsorption measurements; M. L.: DNP experiments, supervision, methodology, funding acquisition, writing, and editing of the manuscript. All authors have contributed to, seen and approved the manuscript.

## Conflicts of interest

There are no conflicts to declare.

## Acknowledgements

We thank Dr Alexander C. Forse for access to the $CO_2$ adsorption measurements. I. B. M. is grateful to the Sustainability and Energy Research Initiative (SAERI) fellowship for financial support. This research was funded by the European Research Council (MIDNP, Grant 803024), the European Union's Horizon 2020 research and innovation program (Pan-European Solid-State NMR Infrastructure for Chemistry-Enabling Access, PANACEA, Grant Agreement 101008500) and the Clore Institute for High Field Magnetic Resonance Spectroscopy and Imaging. Dr Daniel Jardón-Álvarez is acknowledged for valuable discussions and the help with data processing. We also thank Dr Ayan Maity for acquiring the SEM images. The work was made possible in part by the historic generosity of the Harold Perlman family.

## References

1 O. M. Yaghi, M. O'Keeffe, N. W. Ockwig, H. K. Chae, M. Eddaoudi and J. Kim, *Nature*, 2003, **423**, 705–714.
2 H. Furukawa, K. E. Cordova, M. O'Keeffe and O. M. Yaghi, *Science*, 2013, **341**, 1230444.
3 A. Schneemann, V. Bon, I. Schwedler, I. Senkovska, S. Kaskel and R. A. Fischer, *Chem. Soc. Rev.*, 2014, **43**, 6062–6096.
4 A. Kirchon, L. Feng, H. F. Drake, E. A. Joseph and H.-C. Zhou, *Chem. Soc. Rev.*, 2018, **47**, 8611–8638.
5 K. Sumida, D. L. Rogow, J. A. Mason, T. M. McDonald, E. D. Bloch, Z. R. Herm, T.-H. Bae and J. R. Long, *Chem. Rev.*, 2012, **112**, 724–781.
6 J.-R. Li, R. J. Kuppler and H.-C. Zhou, *Chem. Soc. Rev.*, 2009, **38**, 1477–1504.
7 C. A. Trickett, A. Helal, B. A. Al-Maythalony, Z. H. Yamani, K. E. Cordova and O. M. Yaghi, *Nat. Rev. Mater.*, 2017, **2**, 17045.
8 D. T. Sun, L. Peng, W. S. Reeder, S. M. Moosavi, D. Tiana, D. K. Britt, E. Oveisi and W. L. Queen, *ACS Cent. Sci.*, 2018, **4**, 349–356.
9 U. Mueller, M. Schubert, F. Teich, H. Puetter, K. Schierle-Arndt and J. Pastré, *J. Mater. Chem.*, 2006, **16**, 626–636.
10 D. Britt, D. Tranchemontagne and O. M. Yaghi, *Proc. Natl. Acad. Sci. U. S. A.*, 2008, **105**, 11623–11627.
11 M. Ranocchiari and J. A. van Bokhoven, *Phys. Chem. Chem. Phys.*, 2011, **13**, 6388–6396.
12 J. Lee, O. K. Farha, J. Roberts, K. A. Scheidt, S. T. Nguyen and J. T. Hupp, *Chem. Soc. Rev.*, 2009, **38**, 1450–1459.
13 A. Corma, H. García and F. X. Llabrés i Xamena, *Chem. Rev.*, 2010, **110**, 4606–4655.
14 Z. Wang, G. Chen and K. Ding, *Chem. Rev.*, 2009, **109**, 322–359.
15 L. J. Murray, M. Dincă and J. R. Long, *Chem. Soc. Rev.*, 2009, **38**, 1294–1314.
16 Y. Peng, V. Krungleviciute, I. Eryazici, J. T. Hupp, O. K. Farha and T. Yildirim, *J. Am. Chem. Soc.*, 2013, **135**, 11887–11894.
17 H. Wu, J. M. Simmons, Y. Liu, C. M. Brown, X.-S. Wang, S. Ma, V. K. Peterson, P. D. Southon, C. J. Kepert, H.-C. Zhou, T. Yildirim and W. Zhou, *Chem. – Eur. J.*, 2010, **16**, 5205–5214.
18 A. J. Howarth, A. W. Peters, N. A. Vermeulen, T. C. Wang, J. T. Hupp and O. K. Farha, *Chem. Mater.*, 2017, **29**, 26–39.
19 B. E. G. Lucier, Y. Zhang, K. J. Lee, Y. Lu and Y. Huang, *Chem. Commun.*, 2016, **52**, 7541–7544.
20 A. E. Khudozhitkov, S. S. Arzumanov, D. I. Kolokolov and A. G. Stepanov, *J. Phys. Chem. C*, 2021, **125**, 13391–13400.
21 D. I. Kolokolov, A. G. Maryasov, J. Ollivier, D. Freude, J. Haase, A. G. Stepanov and H. Jobic, *J. Phys. Chem. C*, 2017, **121**, 2844–2857.
22 Y. Xiao, Y. Chu, S. Li, Y. Su, J. Tang, J. Xu and F. Deng, *J. Phys. Chem. C*, 2020, **124**, 3738–3746.
23 J. Li, S. Li, A. Zheng, X. Liu, N. Yu and F. Deng, *J. Phys. Chem. C*, 2017, **121**, 14261–14268.
24 X. Kong, E. Scott, W. Ding, J. A. Mason, J. R. Long and J. A. Reimer, *J. Am. Chem. Soc.*, 2012, **134**, 14341–14344.
25 A. C. Forse, P. J. Milner, J.-H. Lee, H. N. Redfearn, J. Oktawiec, R. L. Siegelman, J. D. Martell, B. Dinakar, L. B. Zasada, M. I. Gonzalez, J. B. Neaton, J. R. Long and J. A. Reimer, *J. Am. Chem. Soc.*, 2018, **140**, 18016–18031.
26 S. Chen, B. E. G. Lucier, W. Luo, X. Xie, K. Feng, H. Chan, V. V Terskikh, X. Sun, T.-K. Sham, M. S. Workentin and Y. Huang, *ACS Appl. Mater. Interfaces*, 2018, **10**, 30296–30305.
27 Y. Xiao, S. Li, J. Xu and F. Deng, *Curr. Opin. Colloid Interface Sci.*, 2022, **61**, 101633.
28 V. S. Bajaj, C. T. Farrar, M. K. Hornstein, I. Mastovsky, J. Vieregg, J. Bryant, B. Eléna, K. E. Kreischer, R. J. Temkin and R. G. Griffin, *J. Magn. Reson.*, 2003, **160**, 85–90.
29 T. R. Carver and C. P. Slichter, *Phys. Rev.*, 1953, **92**, 212–213.
30 A. Lesage, M. Lelli, D. Gajan, M. A. Caporini, V. Vitzthum, P. Miéville, J. Alauzun, A. Roussey, C. Thieuleux, A. Mehdi, G. Bodenhausen, C. Copéret and L. Emsley, *J. Am. Chem. Soc.*, 2010, **132**, 15459–15461.
31 A. J. Rossini, A. Zagdoun, M. Lelli, A. Lesage, C. Copéret and L. Emsley, *Acc. Chem. Res.*, 2013, **46**, 1942–1951.
32 A. J. Rossini, A. Zagdoun, M. Lelli, J. Canivet, S. Aguado, O. Ouari, P. Tordo, M. Rosay, W. E. Maas, C. Copéret, D. Farrusseng, L. Emsley and A. Lesage, *Angew. Chem., Int. Ed.*, 2012, **51**, 123–127.

33 T. K. Todorova, X. Rozanska, C. Gervais, A. Legrand, L. N. Ho, P. Berruyer, A. Lesage, L. Emsley, D. Farrusseng, J. Canivet and C. Mellot-Draznieks, *Chem. – Eur. J.*, 2016, **22**, 16531–16538.
34 Z. Guo, T. Kobayashi, L.-L. Wang, T. W. Goh, C. Xiao, M. A. Caporini, M. Rosay, D. D. Johnson, M. Pruski and W. Huang, *Chem. – Eur. J.*, 2014, **20**, 16308–16313.
35 T. Kobayashi, F. A. Perras, T. W. Goh, T. L. Metz, W. Huang and M. Pruski, *J. Phys. Chem. Lett.*, 2016, **7**, 2322–2327.
36 D. Carnevale, G. Mouchaham, S. Wang, M. Baudin, C. Serre, G. Bodenhausen and D. Abergel, *Phys. Chem. Chem. Phys.*, 2021, **23**, 2245–2251.
37 F. Pourpoint, A. S. L. Thankamony, C. Volkringer, T. Loiseau, J. Trébosc, F. Aussenac, D. Carnevale, G. Bodenhausen, H. Vezin, O. Lafon and J. P. Amoureux, *Chem. Commun.*, 2014, **50**, 933–935.
38 T. Iwamoto, H. Masuda, S. Ishida, C. Kabuto and M. Kira, *J. Am. Chem. Soc.*, 2003, **125**, 9300–9301.
39 K.-W. Huang and R. M. Waymouth, *J. Am. Chem. Soc.*, 2002, **124**, 8200–8201.
40 B. Corzilius, V. K. Michaelis, S. A. Penzel, E. Ravera, A. A. Smith, C. Luchinat and R. G. Griffin, *J. Am. Chem. Soc.*, 2014, **136**, 11716–11727.
41 P. Wenk, M. Kaushik, D. Richter, M. Vogel, B. Suess and B. Corzilius, *J. Biomol. NMR*, 2015, **63**, 97–109.
42 M. A. Hope, D. M. Halat, P. C. M. M. Magusin, S. Paul, L. Peng and C. P. Grey, *Chem. Commun.*, 2017, **53**, 2142–2145.
43 T. Wolf, S. Kumar, H. Singh, T. Chakrabarty, F. Aussenac, A. I. Frenkel, D. T. Major and M. Leskes, *J. Am. Chem. Soc.*, 2019, **141**, 451–462.
44 A. Harchol, G. Reuveni, V. Ri, B. Thomas, R. Carmieli, R. H. Herber, C. Kim and M. Leskes, *J. Phys. Chem. C*, 2020, **124**, 7082–7090.
45 S. Haber, Rosy, A. Saha, O. Brontvein, R. Carmieli, A. Zohar, M. Noked and M. Leskes, *J. Am. Chem. Soc.*, 2021, **143**, 4694–4704.
46 A. Mishra, M. A. Hope, G. Stevanato, D. J. Kubicki and L. Emsley, *J. Phys. Chem. C*, 2023, **127**, 11094–11102.
47 A. Karmakar, G. M. Bernard, A. Pominov, T. Tabassum, R. Chaklashiya, S. Han, S. K. Jain and V. K. Michaelis, *J. Am. Chem. Soc.*, 2023, **145**, 4485–4499.
48 B. Thomas, D. Jardón-Álvarez, R. Carmieli, J. van Tol and M. Leskes, *J. Phys. Chem. C*, 2023, **127**, 4759–4772.
49 J. Duan, M. Higuchi, S. Horike, M. L. Foo, K. P. Rao, Y. Inubushi, T. Fukushima and S. Kitagawa, *Adv. Funct. Mater.*, 2013, **23**, 3525–3530.
50 Y. Hua, H. Wang, Q. Li, G. Chen, G. Liu, J. Duan and W. Jin, *J. Mater. Chem. A*, 2018, **6**, 599–606.
51 C. R. Kim, T. Uemura and S. Kitagawa, *Microporous Mesoporous Mater.*, 2014, **195**, 31–35.
52 C. R. Kim, T. Uemura and S. Kitagawa, *Chem. Lett.*, 2014, **43**, 1749–1751.
53 T. Devic, V. Wagner, N. Guillou, A. Vimont, M. Haouas, M. Pascolini, C. Serre, J. Marrot, M. Daturi, F. Taulelle and G. Férey, *Microporous Mesoporous Mater.*, 2011, **140**, 25–33.
54 D. Goldfarb and S. Stoll, *EPR Spectroscopy: Fundamentals and Methods*, Wiley, 2018.
55 S. Stoll and A. Schweiger, *J. Magn. Reson.*, 2006, **178**, 42–55.
56 A. Abragam and B. Bleaney, *Electron Paramagnetic Resonance of Transition Ions*, Oxford University Press, 2012.
57 S. Bin Baek, D. Moon, R. Graf, W. J. Cho, S. W. Park, T.-U. Yoon, S. J. Cho, I.-C. Hwang, Y.-S. Bae, H. W. Spiess, H. C. Lee and K. S. Kim, *Proc. Natl. Acad. Sci. U. S. A.*, 2015, **112**, 14156–14161.
58 D. Jardón-Álvarez and M. Leskes, in *Reference Module in Chemistry, Molecular Sciences and Chemical Engineering*, Elsevier Inc, 2021.
59 S. Björgvinsdóttir, B. J. Walder, A. C. Pinon and L. Emsley, *J. Am. Chem. Soc.*, 2018, **140**, 7946–7951.
60 O. Lafon, M. Rosay, F. Aussenac, X. Lu, J. Trébosc, O. Cristini, C. Kinowski, N. Touati, H. Vezin and J.-P. Amoureux, *Angew. Chem., Int. Ed.*, 2011, **50**, 8367–8370.
61 D. Jardón-Álvarez, G. Reuveni, A. Harchol and M. Leskes, *J. Phys. Chem. Lett.*, 2020, 5439–5445.
62 M. H. Levitt, *Spin Dynamics: Basics of Nuclear Magnetic Resonance*, Wiley, 2nd edn, 2008.
63 W. Morris, C. J. Stevens, R. E. Taylor, C. Dybowski, O. M. Yaghi and M. A. Garcia-Garibay, *J. Phys. Chem. C*, 2012, **116**, 13307–13312.
64 A. J. Rossini, A. Zagdoun, M. Lelli, D. Gajan, F. Rascón, M. Rosay, W. E. Maas, C. Copéret, A. Lesage and L. Emsley, *Chem. Sci.*, 2012, **3**, 108–115.
65 J. Perego, S. Bracco, M. Negroni, C. X. Bezuidenhout, G. Prando, P. Carretta, A. Comotti and P. Sozzani, *Nat. Chem.*, 2020, **12**, 845–851.
66 D. I. Kolokolov, A. G. Stepanov and H. Jobic, *J. Phys. Chem. C*, 2015, **119**, 27512–27520.
67 N. Y. Tan, M. T. Ruggiero, C. Orellana-Tavra, T. Tian, A. D. Bond, T. M. Korter, D. Fairen-Jimenez and J. Axel Zeitler, *Chem. Commun.*, 2015, **51**, 16037–16040.
68 L. Samperisi, A. Jaworski, G. Kaur, K. P. Lillerud, X. Zou and Z. Huang, *J. Am. Chem. Soc.*, 2021, **143**, 17947–17952.
69 A. E. Khudozhitkov, D. I. Kolokolov and A. G. Stepanov, *J. Phys. Chem. C*, 2018, **122**, 12956–12962.
70 H. Babaei, M. E. DeCoster, M. Jeong, Z. M. Hassan, T. Islamoglu, H. Baumgart, A. J. H. McGaughey, E. Redel, O. K. Farha, P. E. Hopkins, J. A. Malen and C. E. Wilmer, *Nat. Commun.*, 2020, **11**, 4010.
71 W. D. C. B. Gunatilleke, K. Wei, Z. Niu, L. Wojtas, G. Nolas and S. Ma, *Dalton Trans.*, 2017, **46**, 13342–13344.
72 B. L. Huang, Z. Ni, A. Millward, A. J. H. McGaughey, C. Uher, M. Kaviany and O. Yaghi, *Int. J. Heat Mass Transfer*, 2007, **50**, 405–411.
73 K. J. Erickson, F. Léonard, V. Stavila, M. E. Foster, C. D. Spataru, R. E. Jones, B. M. Foley, P. E. Hopkins, M. D. Allendorf and A. A. Talin, *Adv. Mater.*, 2015, **27**, 3453–3459.
74 M. Moayed Mohseni, M. Jouyandeh, S. Mohammad Sajadi, A. Hejna, S. Habibzadeh, A. Mohaddespour, N. Rabiee, H. Daneshgar, O. Akhavan, M. Asadnia, M. Rabiee, S. Ramakrishna, R. Luque and M. Reza Saeb, *Chem. Eng. J.*, 2022, **449**, 137700.

75 D. J. Kubicki, A. J. Rossini, A. Purea, A. Zagdoun, O. Ouari, P. Tordo, F. Engelke, A. Lesage and L. Emsley, *J. Am. Chem. Soc.*, 2014, **136**, 15711–15718.
76 D. Le, F. Ziarelli, T. N. T. Phan, G. Mollica, P. Thureau, F. Aussenac, O. Ouari, D. Gigmes, P. Tordo and S. Viel, *Macromol. Rapid Commun.*, 2015, **36**, 1416–1421.
77 C. Landaverde-Alvarado, A. J. Morris and S. M. Martin, *J. CO2 Util.*, 2017, **19**, 40–48.
78 R. Carmieli, P. Manikandan, B. Epel, A. J. Kalb (Gilbo, A. Schnegg, A. Savitsky, K. Möbius and D. Goldfarb, *Biochemistry*, 2003, **42**, 7863–7870.
79 O. S. Leifson and C. D. Jeffries, *Phys. Rev.*, 1961, **122**, 1781–1795.
80 T. Chakrabarty, N. Goldin, A. Feintuch, L. Houben and M. Leskes, *ChemPhysChem*, 2018, **19**, 2139–2142.
81 I. J. Lowe and D. Tse, *Phys. Rev.*, 1968, **166**, 279–291.
82 W. Li, Q. Zhang, J. J. Joos, P. F. Smet and J. Schmedt auf der Günne, *Phys. Chem. Chem. Phys.*, 2019, **21**, 10185–10194.
83 R. Harrabi, T. Halbritter, F. Aussenac, O. Dakhlaoui, J. van Tol, K. K. Damodaran, D. Lee, S. Paul, S. Hediger, F. Mentink-Vigier, S. T. Sigurdsson and G. De Paëpe, *Angew. Chem., Int. Ed.*, 2022, **61**, e202114103.
84 N. Bloembergen, *Physica*, 1949, **15**, 386–426.
85 A. A. Smith, B. Corzilius, A. B. Barnes, T. Maly and R. G. Griffin, *J. Chem. Phys.*, 2012, **136**, 15101.
86 G. Stevanato, D. J. Kubicki, G. Menzildjian, A.-S. Chauvin, K. Keller, M. Yulikov, G. Jeschke, M. Mazzanti and L. Emsley, *J. Am. Chem. Soc.*, 2019, **141**, 8746–8751.
87 Y. Rao, C. T. Palumbo, A. Venkatesh, M. Keener, G. Stevanato, A.-S. Chauvin, G. Menzildjian, S. Kuzin, M. Yulikov, G. Jeschke, A. Lesage, M. Mazzanti and L. Emsley, *J. Phys. Chem. C*, 2022, **126**, 11310–11317.
88 D. Jardón-Álvarez, N. Kahn, L. Houben and M. Leskes, *J. Phys. Chem. Lett.*, 2021, **12**, 2964–2969.
89 M. A. Hope, S. Björgvinsdóttir, D. M. Halat, G. Menzildjian, Z. Wang, B. Zhang, J. L. MacManus-Driscoll, A. Lesage, M. Lelli, L. Emsley and C. P. Grey, *J. Phys. Chem. C*, 2021, **125**, 18799–18809.
90 J. Xu, V. V Terskikh, Y. Chu, A. Zheng and Y. Huang, *Magn. Reson. Chem.*, 2020, **58**, 1082–1090.
91 M. Rauche, S. Ehrling, S. Krause, I. Senkovska, S. Kaskel and E. Brunner, *Chem. Commun.*, 2019, **55**, 9140–9143.
92 D. Massiot, F. Fayon, M. Capron, I. King, S. Le Calvé, B. Alonso, J.-O. Durand, B. Bujoli, Z. Gan and G. Hoatson, *Magn. Reson. Chem.*, 2002, **40**, 70–76.